Supplementary Materials for

A Direct Role for the Sec1-Munc18-Family Protein Vps33 as a Template for SNARE Assembly

Richard W. Baker, Philip D. Jeffrey, Michael Zick, Ben P. Phillips,
William T. Wickner, and Frederick M. Hughson.

correspondence to: hughson@princeton.edu

This PDF file includes:

Materials and Methods
Figs. S1 to S9
Table S1

Materials and Methods

Recombinant protein production

Chaetomium thermophilum Vps33, Vps16, and mutants and truncations thereof were purified as described (*11*). *C. thermophilum* vacuolar SNAREs were identified using reciprocal BLAST searches based on the *Saccharomyces cerevisiae* sequences, yielding *C. thermophilum* Nyv1 (NCBI accession XP_006693724), Vam3 (NCBI Accession XP_006692088), Vam7 (NCBI accession XP_006692683), and Vti1 (NCBI accession XP_006696366). All four SNAREs were cloned from *C. thermophilum* genomic DNA. Plasmids for bacterial overproduction of SNARE motifs (Nyv1 residues 148-212, Vam3 residues 181-245, Vam7 residues 307-371, and Vti1 residues 126-190) as Maltose Binding Protein (MBP) fusion proteins with N-terminal heptahistidine tags were generated using a modified pQLinkH vector (*31*) containing the MBP sequence from pMAL-C (New England BioLabs). Purification protocols for His_7-MBP-SNARE constructs were identical to those used to purify other His-tagged proteins (*11*). The SNARE motifs were purified by anion exchange and size-exclusion chromatography after removing the His_7-MBP tag using recombinant TEV protease. Native and selenomethionine- (SeMet-) derivatized proteins were overproduced in BL21-CodonPlus *Escherichia coli* (Agilent) in Luria-Bertani (LB) medium or in M9 minimal media supplemented with 60 mg/liter SeMet (Sigma), respectively. *S. cerevisiae* HOPS (*18*), Sec17 (*32*), Sec18 (*33*), Ypt7 (*18*), and vacuolar SNAREs (*16, 32, 34, 35*) were purified as previously described.

Crystallization, Data Collection, and Refinement

Vps33–Vps16(505-834)–Vam3(181-245) crystals were grown at 20°C using the sitting drop vapor diffusion method with a 1:1 (v/v) mixture of protein (5 mg/mL Vps33–Vps16(505-834) plus 1.5 molar equivalents of Vam3(181-245)) and precipitant solution (5% w/v Tacsimate (Hampton Research), 0.1 M HEPES pH 7.0, 8-10 % w/v PEG 5000 MME). Crystals were improved using streak seeding and grew to maximum size in approximately 72 h. Crystals were cryoprotected using sequential transfer into mother liquor supplemented with 10, 20, and 30% v/v ethylene glycol. Crystals containing just the Vps33–Vps16(505-834) complex grew under similar conditions. Vps33–Vps16(505-730)–Nyv1(148-212) crystals were grown analogously to Vam3 crystals, using a 1:1 (v/v) ratio of protein (5 mg/ml Vps33–Vps16 plus 1.2 molar equivalents of Nyv1(148-212)) and precipitant solution (0.8 M potassium sodium tartrate, 0.1 M Tris-HCl pH 8.5, 0.5% w/v PEG 5000 MME). Crystals were cryoprotected using a single transfer into mother liquor supplemented by 30% v/v ethylene glycol.

Data were collected on each crystal form at beamline X29 of the National Synchrotron Light Source and processed with the programs HKL (*36*) and autoPROC (*37*). Crystals containing Vps33–Vps16(505-834)–Vam3(181-245) were in space group $P2_1$ with two complexes per asymmetric unit and unit cell dimensions of a = 95.0 Å, b = 95.9 Å, c = 164.1 Å, $\beta = 99.1^\circ$, diffracting to a maximum resolution of 3.1 Å. Vps33–Vps16(505-834) crystallized in space group $P2_1$ with two complexes per asymmetric unit and unit cell dimensions of a = 79.3 Å, b = 159.9 Å, c = 97.4 Å, $\beta = 90.2^\circ$, diffracting to 2.9 Å resolution. This "native" crystal form closely resembled our previously reported

Vps33–Vps16(505-834) structure (PDB entry 4KMO (*11*)) but with more of Vps16 displaying interpretable electron density (see below). Crystals containing a single Vps33–Vps16(505-730)–Nyv1(148-212) complex in the asymmetric unit grew in space group $P2_12_12_1$ with unit cell dimensions of a = 101.0 Å, b = 258.9 Å, c = 75.3 Å, diffracting to 3.1 Å resolution. Data collection and processing statistics for these crystal forms are shown in table S1.

The structures for all three crystal forms were determined by molecular replacement with the program PHASER (*38*) using the previous *C. thermophilum* Vps33–Vps16(505-834) crystal structure (PDB entry 4KMO) as a model. Structures were rebuilt using the program COOT (*39*) and refined using the program phenix.refine (*40*). Non-crystallographic symmetry restraints were used when the crystal contained multiple copies of any monomer. Test set reflections (5% of the total number of reflections) were selected randomly and maintained throughout refinement.

In the new Vps33–Vps16(505-834) structure, Vps16 could be built into well-defined model-phased electron density maps through residue 828, significantly further than previously reported (residue 791 in 4KMO) (*11*). The additional Vps16 ordering, which appears to be due to crystal packing stabilizing the flexible α-solenoid of Vps16, maintains the α-helical repeat motif seen in the rest of this domain. This part of the Vps16 C-terminus is also seen in the Vps33–Vps16(505-834)–Vam3(181-245) complex but is absent from the Vps16 construct used to crystallize Vps33–Vps16(505-730)–Nyv1(148-212). The current model of Vps33–Vps16(505-834) has a good fit to the data (table S1) and contains Vps33 residues 5-272, 296-542, 558-585, and 599-657; Vps16 residues 532-828; and two D-malate ions from the crystallization medium.

The model-phased difference map arising from the molecular replacement solution of the Vps33–Vps16(505-834)–Vam3(181-245) crystal form showed clear features for two long α-helices packing against domain 3a of Vps33. After building of the polypeptide backbone, these α-helices were identified by connectivity and sequence assignment as being Vam3 residues 188-213 and Vps16 residues 505-526, the latter originating from an adjacent complex in the crystal lattice (fig. S2). The Vam3 sequence assignment was made from difference electron density maps after the helical backbone was built. Twenty-two TLS groups were refined. The current model has an excellent fit to the data (table S1) and contains Vps33 residues 5-272, 296-545, 556-582, and 599-658; Vps16 residues 505-828; and Vam3 residues 188-225.

The model-phased difference map arising from the molecular replacement solution of the Vps33–Vps16(505-730)–Nyv1(148-212) crystal form showed density for a pair of helices packing along Vps33 domain 3a, one of which mediated crystal packing between the tips of Vps33 domain 3a in two adjacent but equivalent Vps33 molecules (fig. S3). Necessarily this helix is therefore 2-fold disordered about a crystallographic two-fold axis. Its location indicated that it must be from Nyv1 as there were no other alternative polypeptide chains nearby. Furthermore anomalous difference maps after labeling Nyv1 with SeMet showed a peak for the endogenous Met 170 (see below). We refer to this helix as Nyv1(165-179). This packing interface is a critical one tying the crystal lattice together and its relatively small extent may be the root cause of the relatively high average B-factors (117 $Å^2$) in the Nyv1 complex structure. We modeled this helix with an occupancy of 0.5 since one helix is sandwiched between two Vps33 molecules. The second Nyv1 helix corresponds to residues 183-202, an assignment guided by Leu to Met

point mutations (L186M, L187M) in Nyv1(148-212) and confirmed by the collection of single wavelength anomalous scattering data on SeMet-labeled Nyv1 at the selenium K edge (λ=0.9793 Å) and calculation of model-phased log-likelihood gradient (LLG) anomalous difference maps (figure S3D). A peak corresponding to endogenous Met 170 was also observed adjacent to the Nyv1(165-179) helix.

Since the Vps33–Vps16(505-730)–Nyv1(148-212) crystal structure lacked non-crystallographic symmetry, we applied additional restraints in the later stages of refinement by using a reference model constructed from the homologous Vps33–Vps16(505-834) and Vps33–Vps16(505-834)–Vam3(181-245) structures in backbone regions where these structures were essentially identical. Eight TLS groups were refined. The current model has an excellent fit to the data (table S1) and contains Vps33 residues 5-272, 296-543, 556-582, and 599-659; Vps16 residues 524-730; and Nyv1 residues 165-179 and 183-202. The sequence register of Nyv1 residues 165-179 should be considered provisional, given the disorder detailed above.

Simulated annealing omit maps were calculated for each Vps33–Vps16–SNARE complex by setting the occupancies of all SNARE atoms to zero and performing torsion angle simulated annealing refinement with a starting temperature of 2500K (figures S2C, S3E).

Binding Assays

Proteins were mixed at a final concentration of 50 μM each and incubated at room temperature for 1 h. 500 μL was then run on a Superdex 200 10/300 Increase column (GE Healthcare) equilibrated with 20 mM Tris-HCl pH 7.5, 250 mM NaCl, 1 mM DTT.

Yeast Strain Construction

A centromeric plasmid containing a C-terminally GFP tagged Vps33 under the control of its endogenous promoter (pRS416-Vps33-GFP) was generously provided by Dr. Alexey Merz (*4*). Vps33 mutations were introduced using site-directed mutagenesis. The resulting plasmids were transformed using the lithium acetate method (*41*) into a Vps33 null yeast strain AMY1275 (BY4742; *vps33Δ*::KAN (*4*)).

HOPS overexpression strains were created essentially as described (*42*). Briefly, mutations were introduced onto a Vps33 expression plasmid (p403-GAL1-Vps33-TEV-GST) and transformed into the strain CHY38, which has five HOPS subunits (Vps11, Vps16, Vps18, Vps39, Vps41) under control of the *GAL1* promoter. The resultant strains overexpressed all six HOPS subunits and produced a complex wild-type in all aspects except for the mutations in Vps33.

In vivo vacuole morphology

5 mL overnight cultures were grown from a single yeast colony in synthetic complete media lacking uracil. Saturated cultures were back diluted to OD_{600} = 0.001 and grown overnight at 30°C. Cultures in mid-log phase were incubated with 3 μM FM4-64 (Life Technologies) for 15 min at 30°C. Cells were centrifuged for 30 s at 800 g, washed with fresh media, and incubated at 30°C for at least 60 min before plating on a microscope slide. Cells were imaged on a DeltaVision deconvolution microscope (Applied Precision) with an inverted 100x NA 1.4 objective and a Cool Snap HQ CCD camera (Photometrics). Images were deconvolved using the Applied Precision SoftWoRx

imaging software. Vacuole morphology was determined for 150-350 cells per experiment per strain. Cells were classified as wild-type if they contained 1-3 large, circular vacuoles; cells were classified as having vacuolar fusion defects if they contained 4 or more vacuoles.

Reconstitution of vacuolar Rab/SNARE proteoliposomes

Proteoliposomes were prepared from mixed micellar solutions (containing 50 mM β-octyl-glucoside and either 4 μM biotinylated R-phycoerythrin (Life Technologies) or 8 μM Cy5-derivatized streptavidin (KPL)) by detergent dialysis (20 kDa cutoff membrane) in RB150/Mg^{2+} (20 mM HEPES-NaOH pH 7.4, 150 mM NaCl, 1 mM $MgCl_2$, 10% glycerol (v/v)) as described (*18*). Lipids dissolved in chloroform were mixed at the following proportions: 44.6 - 47.6 mol% DLPC (1,2-dilinoleoyl-*sn*-glycero-3-phosphocholine), 18 mol% DLPE (1,2-dilinoleoyl-*sn*-glycero-3-phosphoethanolamine), 18 mol% Soy PI (L-α-phosphatidylinositol), 4.4 mol% DLPS (1,2-dilinoleoyl-*sn*-glycero-3--phospho-L-serine), 2 mol% DLPA (1,2-dilinoleoyl-*sn*-glycero-3-phosphate), 1 mol% 16:0 DAG (1,2-dipalmitoyl-*sn*-glycerol), 8 mol% ergosterol, and 1 mol% PI(3)P (1,2-dipalmitoyl-*sn*-glycero-3-phospho-(1′-myo-inositol-3′-phosphate)). Fluorescent lipids (0.2 mol% Marina-Blue-DHPE or 3 mol% NBD-DHPE) were included to allow parallel assays of lipid mixing (not shown). Lipids were obtained from Avanti Polar Lipids, except that ergosterol was from Sigma-Aldrich, PI(3)P was from Echelon Biosciences, and the fluorescent lipids (Marina-Blue-DHPE, NBD-DHPE) were from Life Technologies. Molar protein:lipid ratios were 1:2000 - 1:32,000 for SNAREs and 1:2,000 for Ypt7, which was present on all proteoliposomes used in this study. Isolation after reconstitution was achieved by flotation on a 3-step Histodenz gradient (35%, 25% Histodenz (w/v), and RB150/Mg^{2+}).

Reconstituted proteoliposome (RPL) fusion assays

In vitro fusion assays were performed using RPLs containing lumenal Cy5-streptavidin or biotinylated R-phycoerythrin (*16*). Upon fusion, the lumenal contents mix, streptavidin tightly binds biotin, and the resulting close proximity of Cy5 and R-phycoerythrin can be assayed as fluorescence resonance energy transfer (FRET). Assays contained external, unlabeled streptavidin to suppress any signal from extra-lumenal complex formation (e.g. due to lysis). Purified HOPS containing wild-type or mutant Vps33 was compared to the artificial tethering factor polyethylene glycol (PEG).

Fusion reactions were assembled in 20 μl. Fusion assay pairs of RPLs (each 250 μM lipid) in RB150, 5 μM streptavidin, 1 mM EDTA, and 10 μM GTP were pre-incubated for 10 min at 27°C prior to addition of 1.25 mM $MgCl_2$ to exchange Ypt7 to its GTP-bound form. Then, 10 μl were transferred to wells of 384-well plates. Soluble components (10 μl of e.g. HOPS, Sec17, Sec18, ATP, Vam7, Vam7ΔPX) or their respective buffers were added to initiate the reactions, either as one addition, or two consecutive 5 μl additions. All reactions contained 0.5% (w/v) defatted BSA, 5 mM reduced glutathione, and 1 mM dithiothreitol. Plates were incubated at 27°C in a SpectraMax Gemini XPS (Molecular Devices) fluorescence plate reader for 30 min and content mixing signals (PhycoE:Cy5-FRET – Ex: 565 nm; Em: 670 nm; cutoff: 630 nm) were recorded at intervals of 10 to 30 s. Maximal values were determined after addition of 0.1% (w/v) Thesit to samples that had not received streptavidin.

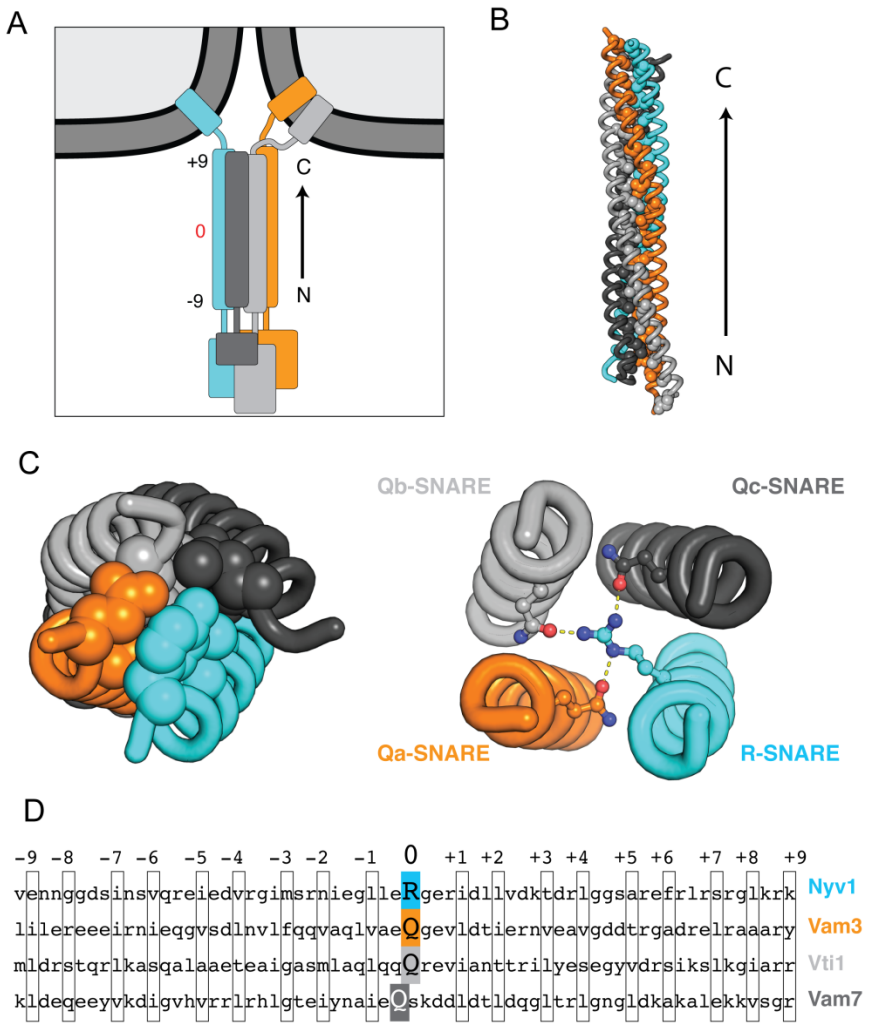

Fig. S1. SNARE complex structure and nomenclature

(**A**) Cartoon depicting a SNARE complex prior to membrane fusion. The SNARE motifs are shown as a fully zippered parallel four-helix bundle (see panel **B**). As depicted, each SNARE also contains an N-terminal domain and, in three out of four cases, a transmembrane anchor. Numbers refer to core layer residues (see panel **D**). (**B**) Crystal structure of neuronal SNARE motifs (PDB code 1SFC) (*43*) assembled in a four-helix bundle. (**C**) The core of the four-helix bundle is primarily composed of hydrophobic amino acids. The zero-layer residues – arginine and glutamine (or occasionally serine) (*2*) – are exceptions, with their interaction thought to ensure that the four SNARE motifs assemble in-register. Qa-, Qb-, and Qc-SNAREs are defined by their relative position within the bundle (here viewed from the C-terminal end). (**D**) Shown are the sequences of the *C. thermophilum* SNARE motifs used in this work. The residues predicted to constitute layers -9 to +9 of the generally hydrophobic core of the four-helix SNARE bundle are boxed. It is unknown whether the Qc-SNARE Vam7 uses the highlighted glutamine residue, or the adjacent serine, as its zero-layer residue.

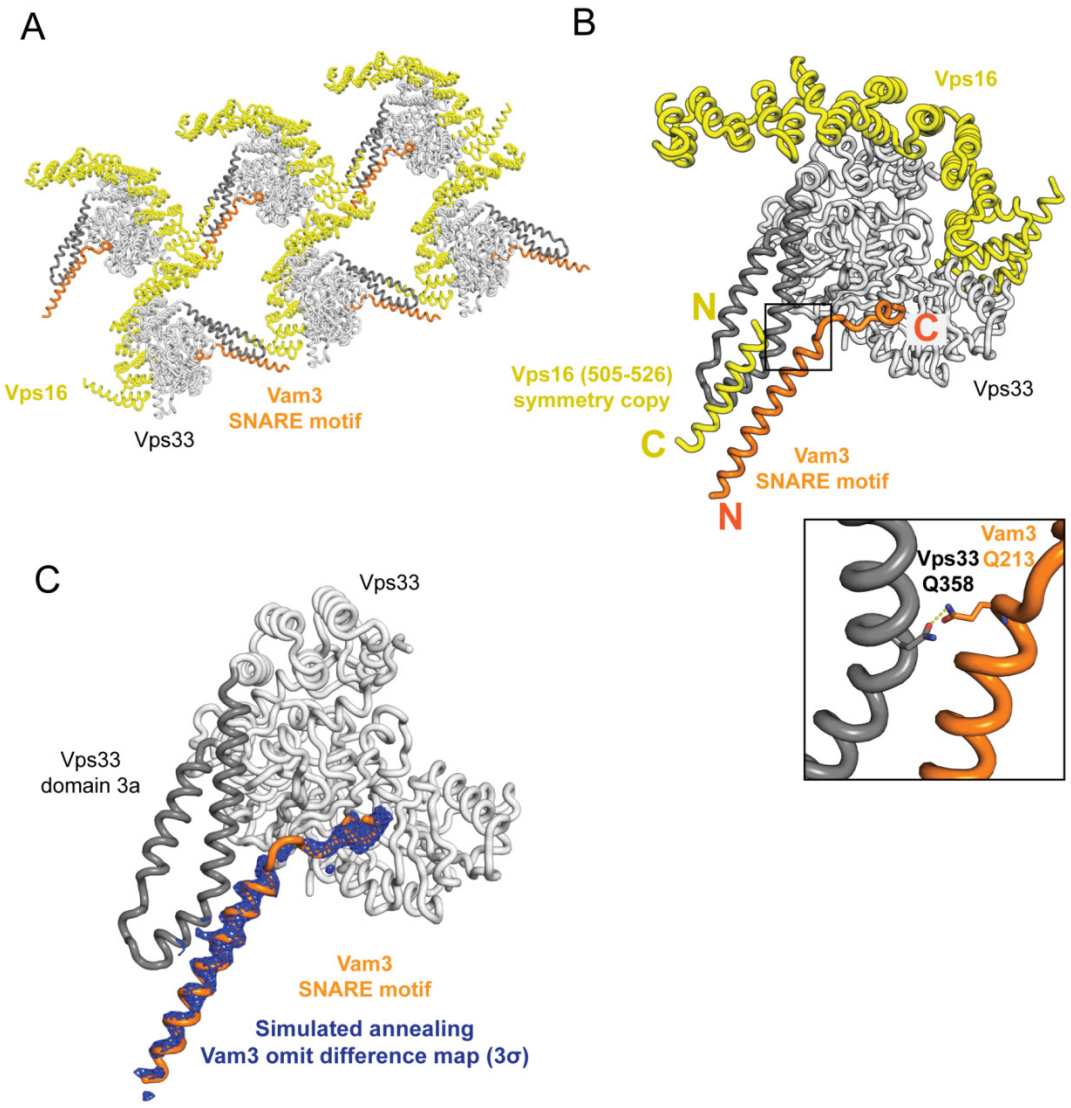

Fig. S2. Structure of Vps33–Vps16(505-834)–Vam3(181-245)

In the crystal structure of the Vps33–Vps16(505-834)–Vam3(181-245) complex, we were able to model a central region (residues 188-225) of the Vam3 SNARE motif into defined electron density (Fig. 1, A and C). (**A**) Crystal lattice. (**B**) Vam3 binds within the cleft formed by the arch-shaped Vps33. Vam3 residues 188-213, including the zero-layer glutamine (Q213), adopt an α-helical conformation that interacts primarily with one of the two long, antiparallel α-helices of Vps33 domain 3a (Fig. 1, B and C). In our crystals, a third α-helix, supplied adventitiously by the Vps16 N-terminus of an adjoining complex, contributes to the formation of a three-helix bundle. Q213 forms an H-bond with the conserved Vps33 residue Q358 (see inset). The remainder of the Vam3 SNARE motif, residues 214-225, comprises a short extended region followed by a short α-helix. (**C**) Simulated annealing omit map for Vam3, contoured at 3σ; at a lower contour level, continuous electron density is observed.

As noted in the text, the SNARE motif of Vam3 binds to Vps33 in a conformation that is similar to the corresponding region of syntaxin1a bound to Munc18a (Fig. 1, C to E, and

fig. S4a) (*7, 8*). The key interactions between Vam3 residues 214-225 and Vps33 are conserved in the syntaxin1a-Munc18a complex. Both SM proteins use an α-helix macrodipole to stabilize an aspartate residue (D218 in Vam3, D231 in syntaxin1a) and a hydrophobic pocket to accommodate an isoleucine residue (I220 in Vam3, I233 in syntaxin1a). N-terminal to the zero-layer residue Q213, the conformations of the two Qa-SNAREs are similar but their interactions with the corresponding SM protein are different. This difference arises from the folding back of the Munc18a helical hairpin, which would otherwise clash with the auto-inhibitory N-terminal Habc domain of syntaxin1a (Fig. 1D and fig. S4) (*14*). Intact Vam3, like syntaxin1a, contains an Habc domain (Fig. 1A); however, Vam3 does not appear to form a stable closed conformation, at least on its own (*10*).

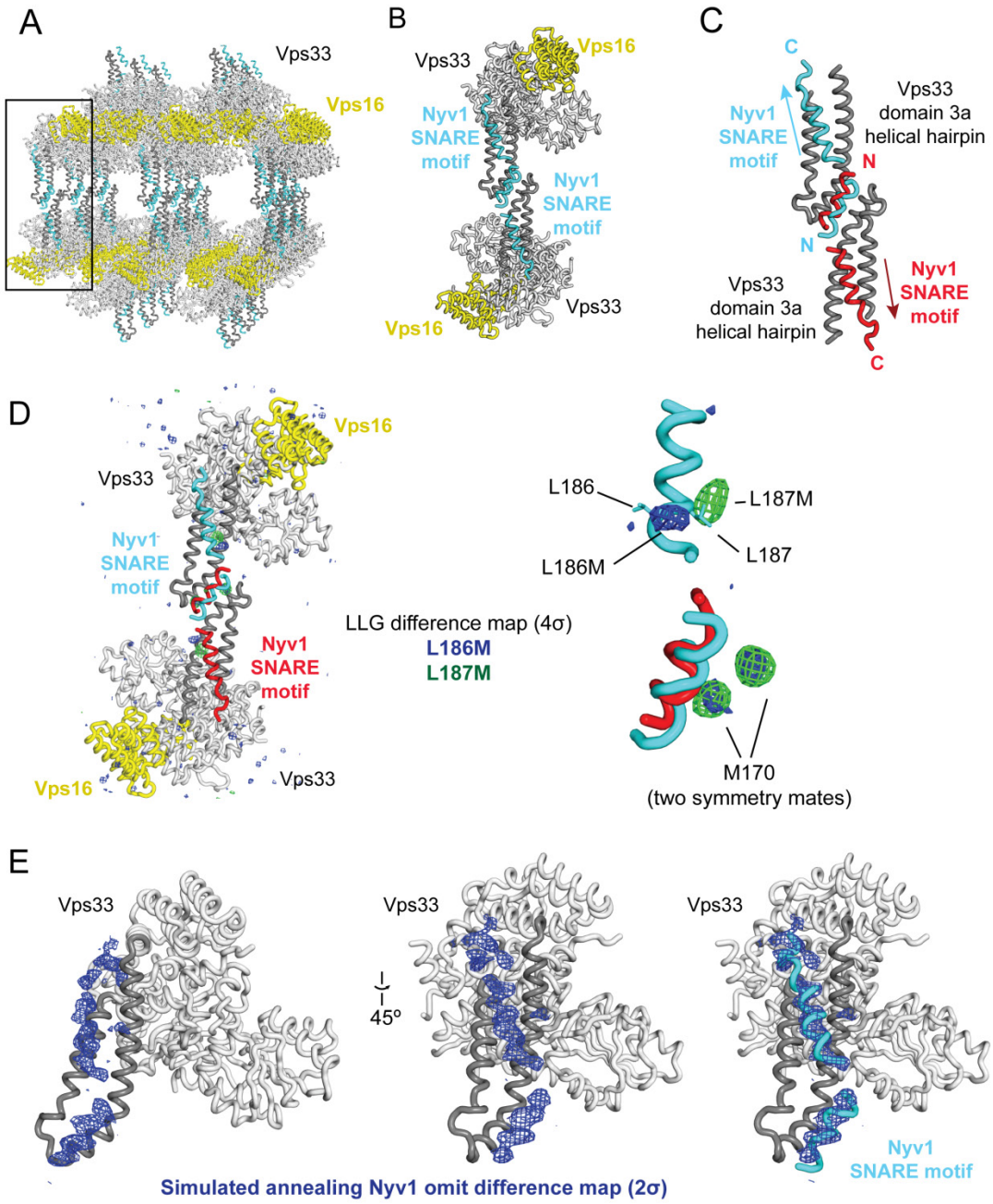

Fig. S3. Structure of Vps33–Vps16(505-730)–Nyv1(148-212)

In the crystal structure of the Vps33–Vps16(505-730)–Nyv1(148-212) complex, a central portion of the Nyv1 SNARE motif was modeled into difference electron density in two segments with a small break corresponding to the zero-layer arginine (R180) and several adjacent residues (Figs. 1A and 2A). The more N-terminal of the modeled Nyv1 segments is a helix (residues 165-179) that superimposes onto a symmetry-related copy of itself and has therefore been modeled as poly-alanine; its sequence register should be considered provisional (see Materials and Methods). The longer and more C-terminal of these segments corresponds to residues 183-202, an assignment validated by

selenomethionine derivatization. (**A**) Crystal lattice. (**B** and **C**) Detailed views illustrating the superimposition of the N-terminal α-helix of Nyv1 on the N-terminal α-helix of Nyv1 in a symmetry-related complex (colored red in **C**). Since both helices cannot occupy the same space simultaneously, one of them per crystal contact must be displaced and thus, presumably, disordered. (**D**) Two copies of the asymmetric unit are shown as in panel **B**, with the addition of the log-likelihood gradient (LLG) anomalous difference maps for SeMet-substituted Nyv1 L186M and L187M. In a closeup view of the Vps33-Nyv1 crystal contact, the orientation and sequence register of the Nyv1 helix (183-202) can be unambiguously determined using the peaks corresponding to the location of the Se atoms. An endogenous Nyv1 methionine, M170, demonstrates that the Nyv1 peptide extends across the entire helical hairpin of Vps33 domain 3a. (**E**) Simulated annealing omit map for Nyv1. The domain 3a helical hairpin of Vps33 is indicated in dark gray. At a contour level of 2σ, as shown, electron density is continuous except for a break around the zero-layer R180.

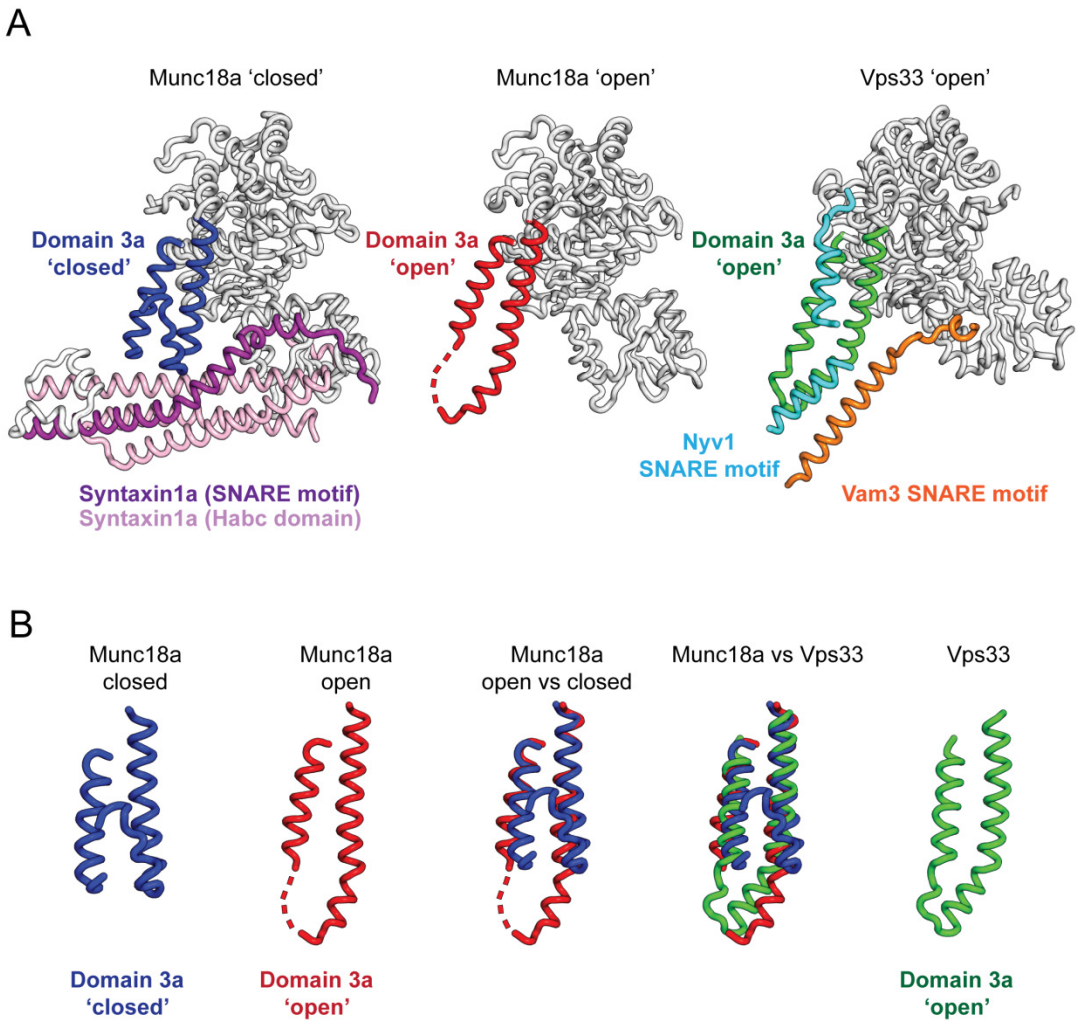

Fig. S4. Vam3-bound Vps33 adopts an open, R-SNARE-receptive conformation also observed for Munc18a

(**A**) In the Munc18a–syntaxin1a complex (PDB code 3C98), the syntaxin Habc domain forces the domain 3a helical hairpin into a folded-back closed (or 'furled') conformation (*7, 8, 44*). By contrast, the helical hairpin is extended or 'open' in all of the Vps33 structures reported here, and also in uncomplexed Munc18a (*14*). It is attractive to speculate that the priming factor Munc13 disengages the Habc domain, removing the steric block to helical hairpin opening (*26*). In its open conformation, the helical hairpin is then able to bind the R-SNARE. (**B**) The open conformations of Munc18a and Vps33 are similar (see also (*11, 14*)).

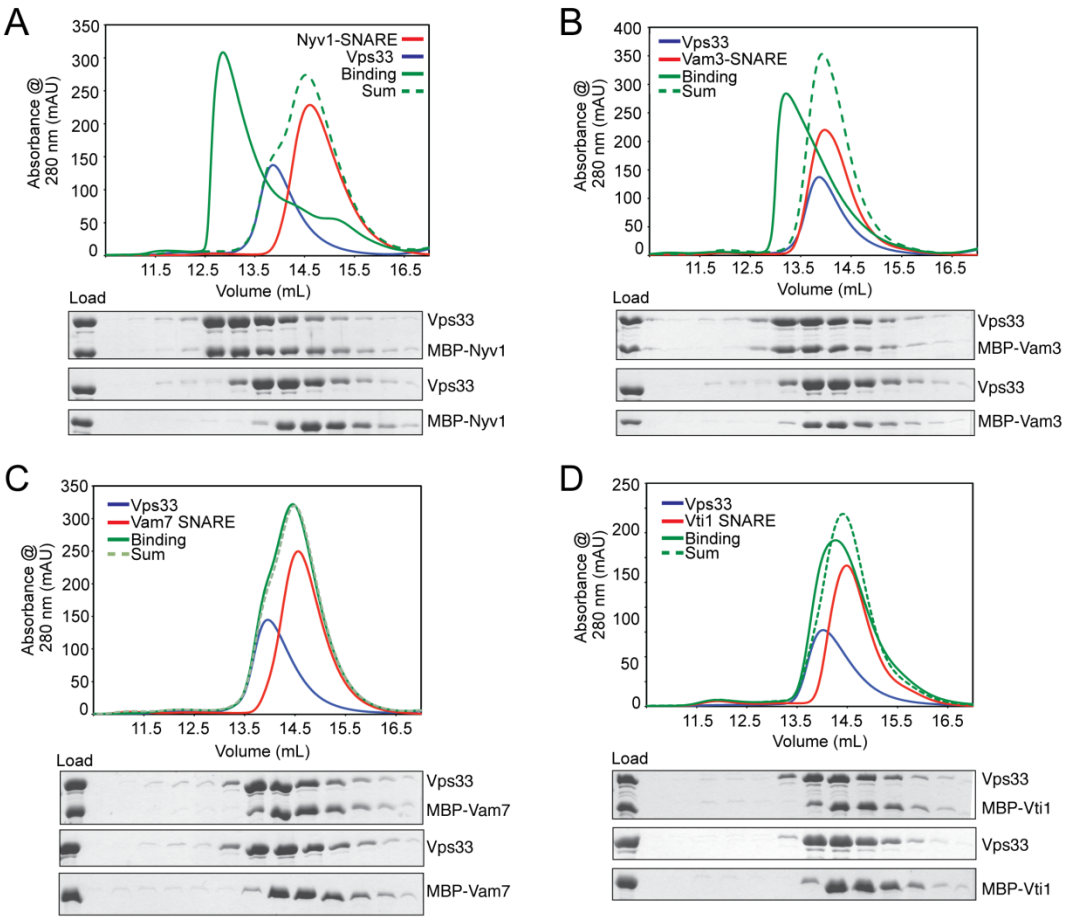

Fig. S5. *C. thermophilum* Vps33 binding to SNARE motifs

(**A** - **D**) Size exclusion chromatography was used to analyze individual proteins and binary combinations; shown for comparison is the sum of the chromatograms for the individual proteins. Complex formation is indicated by earlier elution, consistent with larger molecular size. (**A**) Vps33 binds to the R-SNARE MBP-Nyv1(148-212). (**B**) Vps33 binds to the Qa-SNARE MBP-Vam3(181-245). (**C**) Vps33 does not bind to the Qc-SNARE MBP-Vam7(307-371). (**D**) Vps33 does not bind to the Qb-SNARE MBP-Vti1(126-190).

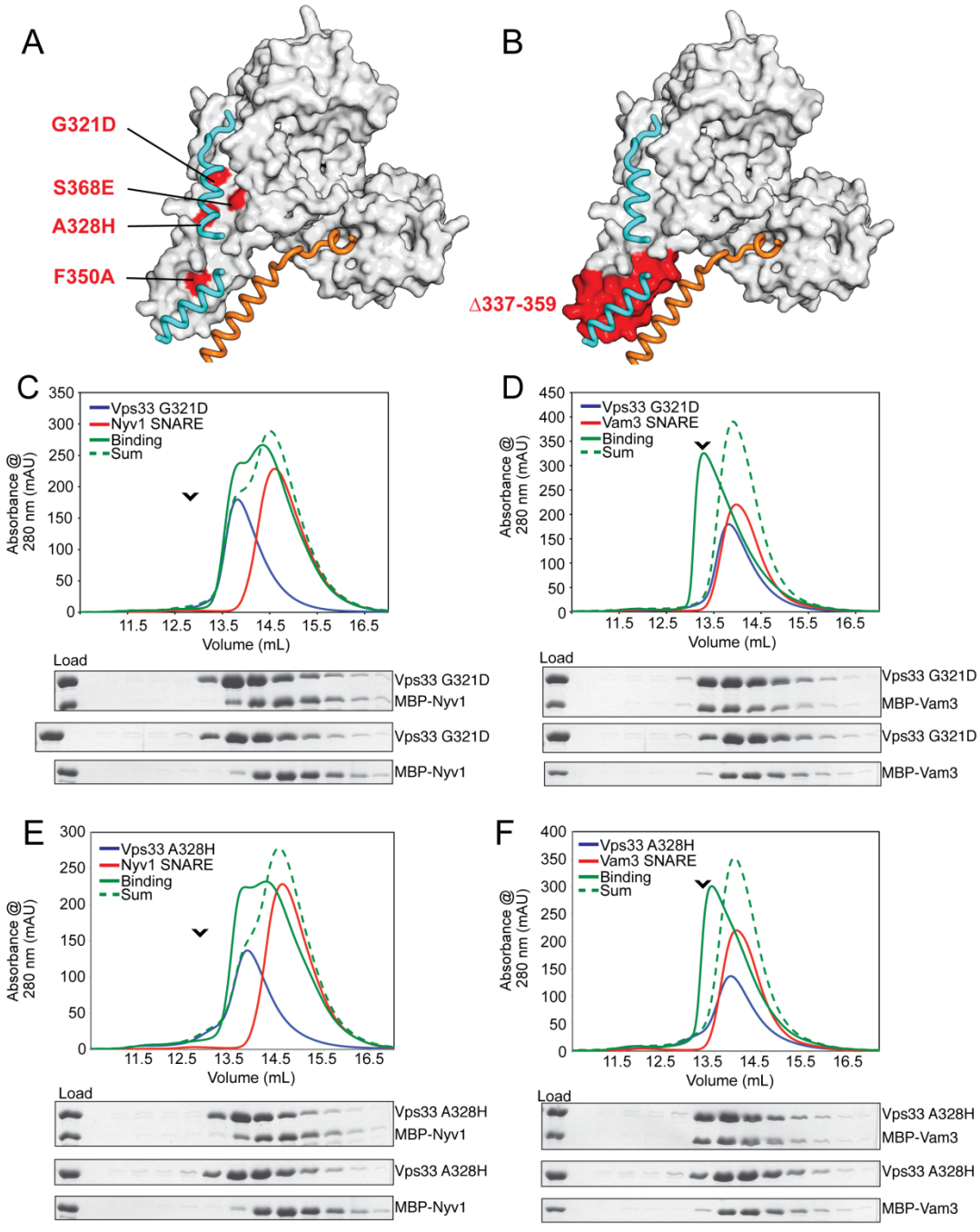
A
G321D
S368E
A328H
F350A
B
Δ337-359
C
Vps33 G321D
Nyv1 SNARE
Binding
Sum
Absorbance @ 280 nm (mAU)
Volume (mL)
Load
Vps33 G321D
MBP-Nyv1
D
Vps33 G321D
Vam3 SNARE
Binding
Sum
Absorbance @ 280 nm (mAU)
Volume (mL)
Load
Vps33 G321D
MBP-Vam3
E
Vps33 A328H
Nyv1 SNARE
Binding
Sum
Absorbance @ 280 nm (mAU)
Volume (mL)
Load
Vps33 A328H
MBP-Nyv1
F
Vps33 A328H
Vam3 SNARE
Binding
Sum
Absorbance @ 280 nm (mAU)
Volume (mL)
Load
Vps33 A328H
MBP-Vam3

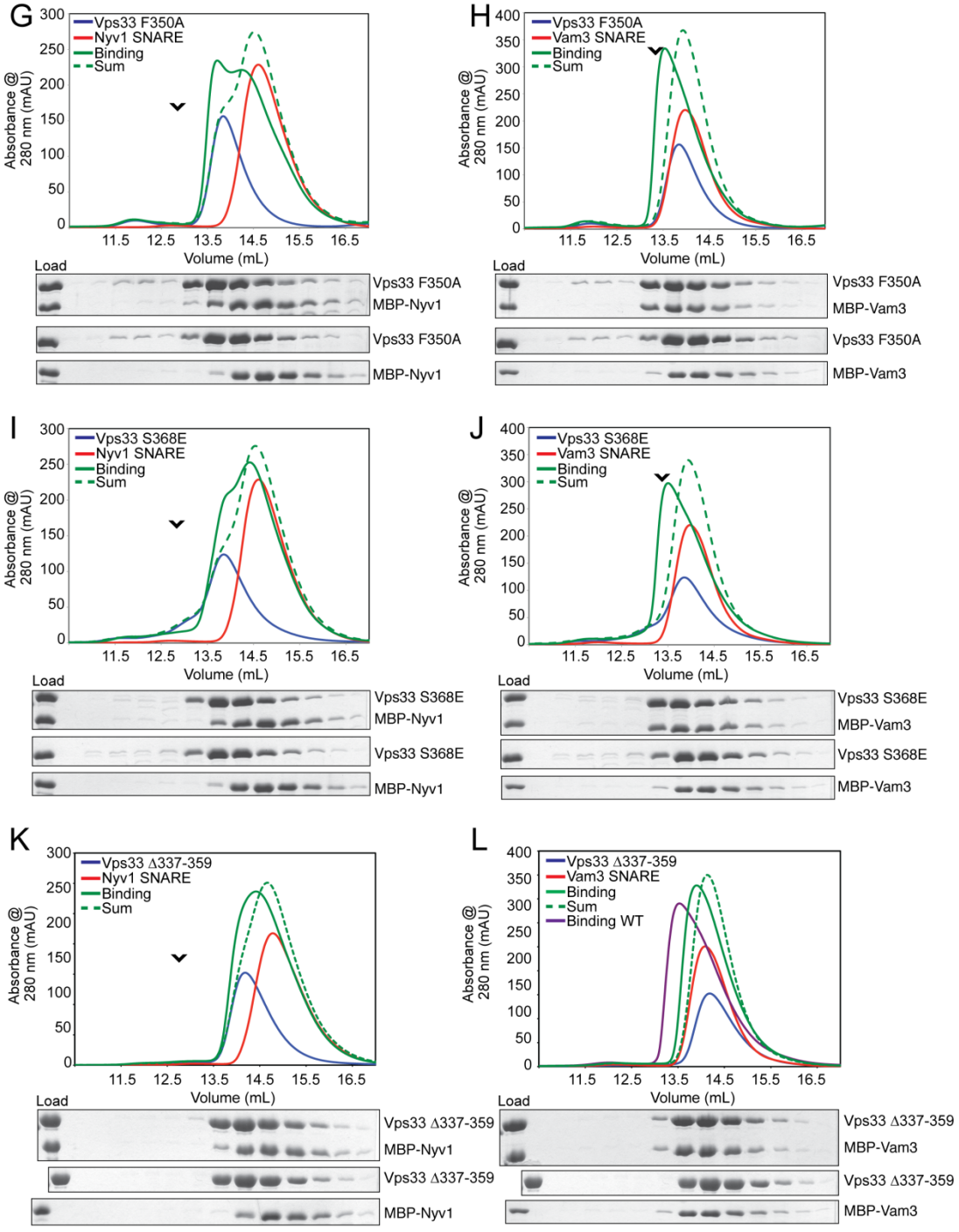

Fig. S6. Mutant *C. thermophilum* Vps33 binding to Nyv1 and Vam3 SNARE motifs
(**A** and **B**) *C. thermophilum* Vps33 mutants tested – the locations of the mutated or deleted residues are shown in red. (**C - L**) Complex formation was evaluated by size exclusion chromatography as in fig. S5; the elution position of the corresponding wild-type complexes are indicated with carets. All of the Vps33 mutants tested strongly

compromised binding to the R-SNARE MBP-Nyv1(148-212). Binding to the Qa-SNARE MBP-Vam3(181-245) was unaffected by the point mutation Vps33(G321D) (equivalent to *S. cerevisiae* Vps33(G338E)) but was nearly abolished by the deletion Vps33(Δ337-359) (equivalent to *S. cerevisiae* Vps33(Δ354-376)). Other mutants displayed intermediate elution volumes, probably signifying the dissociation of lower affinity complexes while passing through the size exclusion column.

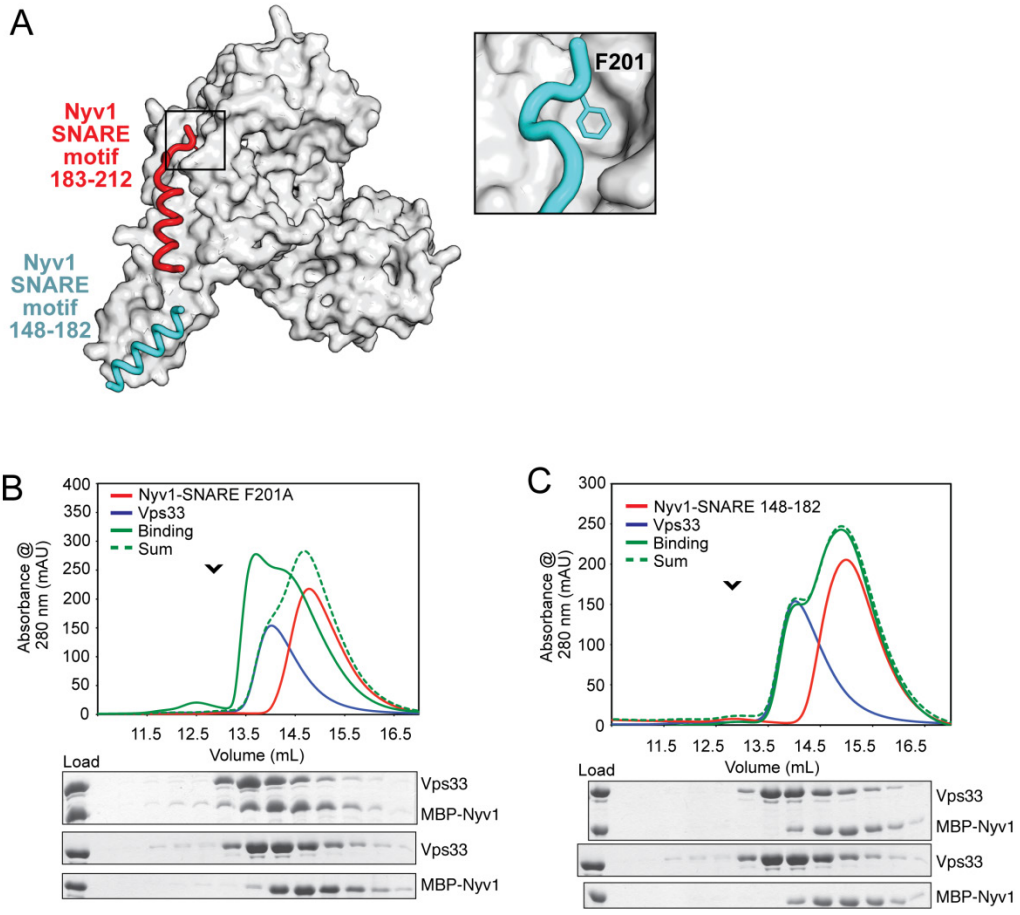

Fig. S7. Vps33 binding to mutant Nyv1 SNARE motif

(**A**) *C. thermophilum* Nyv1 SNARE motif constructs tested. (**B** and **C**) Complex formation was evaluated by size exclusion chromatography as in fig. S5; the elution position of the corresponding wild-type complexes are indicated with carets. (**B**) The point mutation F201A compromises binding of MBP-Nyv1(148-212) to Vps33. (**C**) The N-terminal region of the Nyv1 SNARE motif (residues 148-182) does not bind to Vps33.

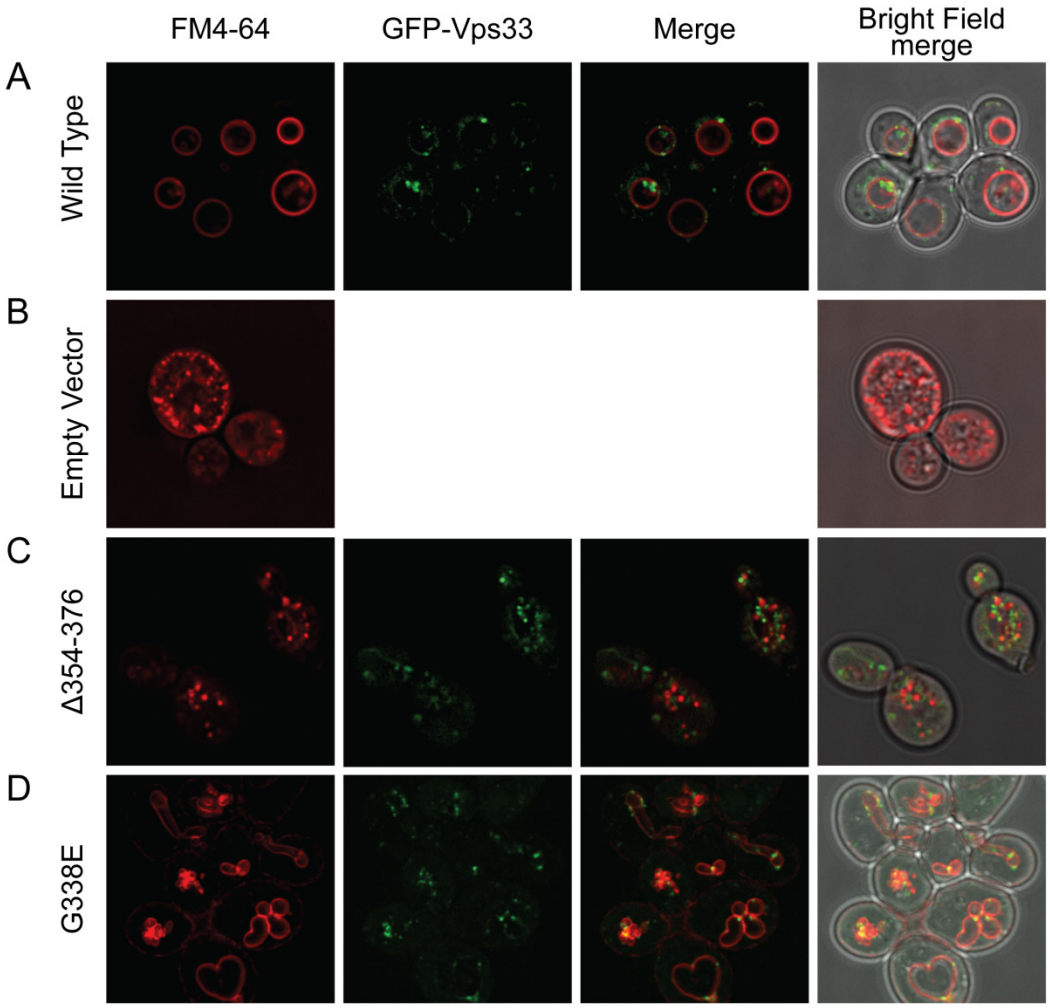
FM4-64
GFP-Vps33
Merge
Bright Field merge
A
Wild Type
B
Empty Vector
C
Δ354-376
D
G338E

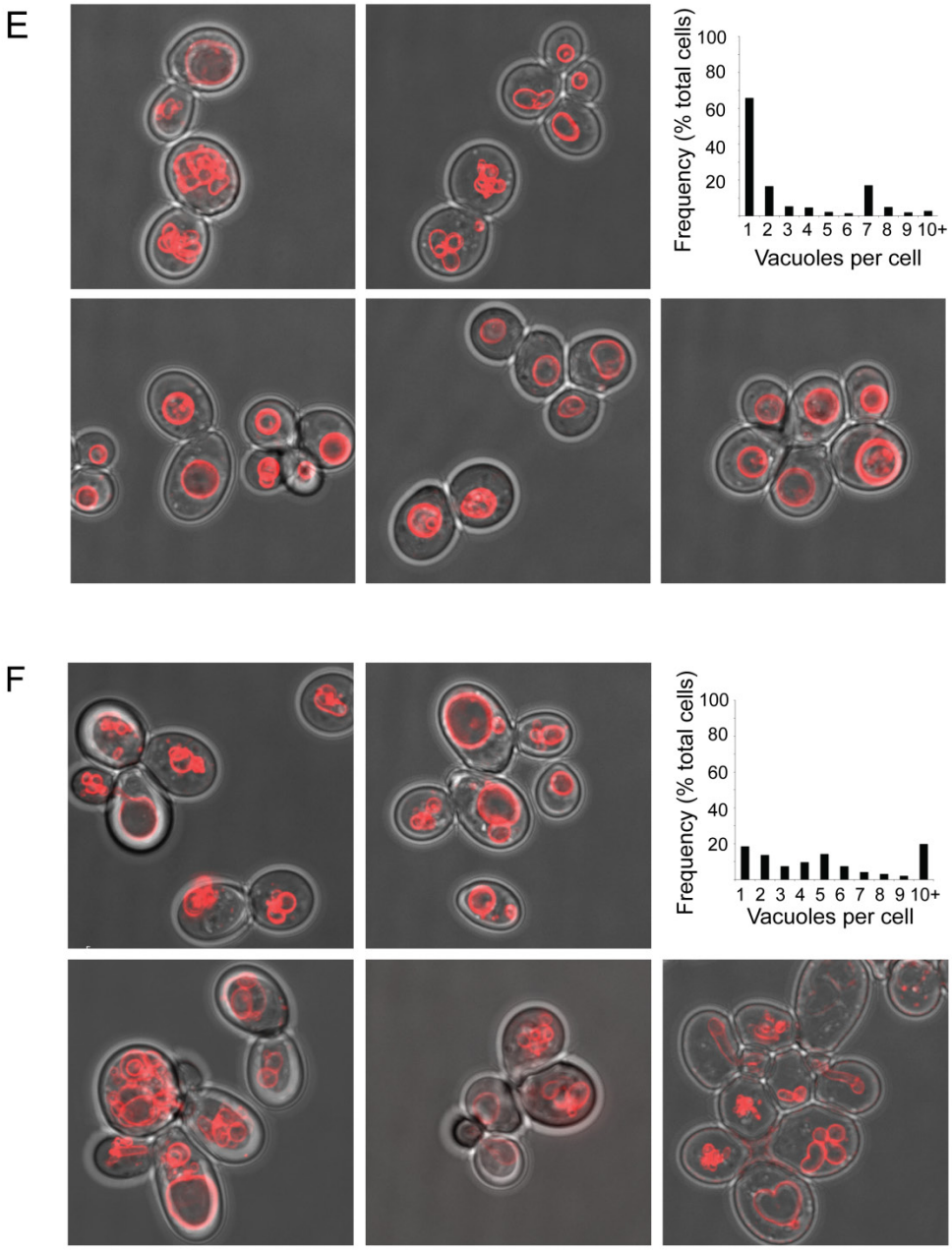

Fig. S8. In vivo fluorescence microscopy of Vps33 mutant yeast strains

(**A** - **D**) Δ*vps33* yeast were transformed with plasmids encoding wild-type or mutant GFP-tagged *S. cerevisiae* Vps33, as in Fig. 3A. Fluorescence and bright field images are shown for (**A**) wild-type *VPS33-GFP*, (**B**) empty vector, (**C**) *vps33(Δ337-359)*, and (**D**) *vps33(G338E)*. *Δvps33* and *vps33(Δ337-359)* strains always displayed diffuse or punctate FM4-64 staining. (**E** - **F**) Additional images of FM4-64 staining are shown for (**E**) *VPS33-GFP* and (**F**) *vps33(G338E)*. Histograms were created by counting vacuoles for all of the cells that were imaged in the three independent experiments reported in Fig. 3A.

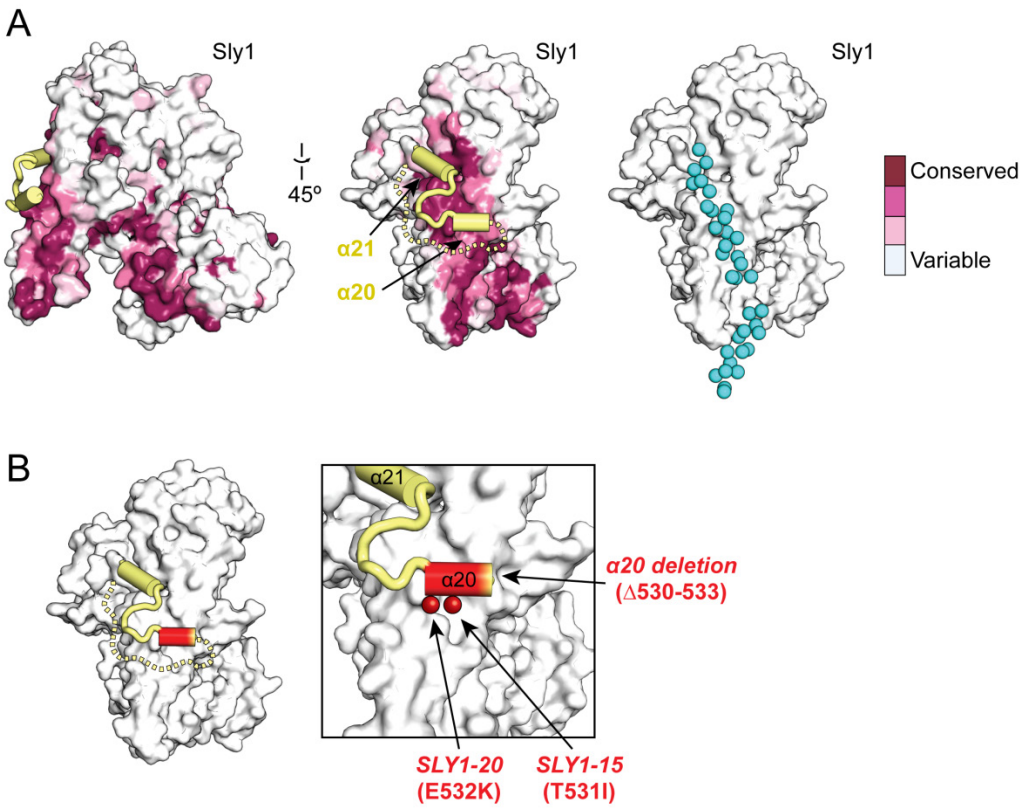

Fig. S9. Potential regulation of R-SNARE binding to the SM protein Sly1

(**A**) An insertion (yellow) within domain 3 of the SM protein Sly1 (PDB code 1MQS) (*27*) lies across – and potentially regulates access to – the presumptive R-SNARE binding groove (indicated by cyan spheres based on the Vps33–Nyv1 structure). Sequence conservation as calculated by ConSurf (*30*) is displayed on the surface of Sly1 generated by excluding the insertion. (**B**) Dominant gain-of-function mutations within the Sly1 insert, including point mutations (red spheres) and a deletion of most of helix α20, relieve the requirement for other regulatory factors including the Rabs Ypt1 and Ypt6 and the tethering complex component Sec35/Cog2 (*29*).

Table S1. Data Collection and Refinement Statistics

Structure	Vps33/Vps16	Vps33/Vps16/Vam3	Vps33/Vps16/Nyv1
Data Collection			
Resolution (Å)	83 – 2.9	50 – 3.05	50 – 3.1
Outer Shell (Å)	2.91 – 2.90	3.21– 3.05	3.27 – 3.10
Observations	300,496	199,822	264,597
Unique Reflections	53,085	54,737	36,792
Redundancy	5.7 (5.8)	3.7 (3.6)	7.2 (7.1)
Completeness	0.99 (0.98)	0.98 (0.85)	1.00 (1.00)
$<I/\sigma_I>$	16.9 (2.1)	10.5 (1.2)	18.5 (2.8)
R_{merge}	0.085 (0.807)	0.102 (0.798)	0.077 (0.648)
R_{meas}	0.095 (0.885)	0.120 (0.938)	0.083 (0.699)
R_{pim}	0.039 (0.362)	0.062 (0.489)	0.031 (0.260)
$CC_{1/2}$	0.998 (0.742)	0.996 (0.632)	0.999 (0.887)
Refinement			
Resolution (Å)	62 – 2.9	50 – 3.1	50 – 3.1
R_{work}	0.212	0.203	0.193
R_{free}	0.276	0.231	0.240
No. of reflections	53,034	53,126	36,708
No. of atoms	14,259	15,276	6,659
RMS Δbond (Å)	0.006	0.003	0.005
RMS Δangle (^{o})	1.06	0.77	1.06
RMS B-factor (Å^2)	4.7	5.0	10.8
Average B-factor (Å^2)			
Vps33	63.5, 62.2	94.3, 94.8	115.6
Vps16	70.4, 81.8	129.3, 120.0	104.3
Vam3 or Nyv1	n/a	158.1, 151.0	196.1
Ramachandran Plot			
Favored (%)	91.9	91.5	90.6
Outliers (%)	1.1	1.6	2.8
PDB code	5BV1	5BUZ	5BV0

Values in parentheses correspond to the highest-resolution shell. The average of the refined atomic B-factors is reported on a per-chain basis either from refined isotropic B-factors (Vps33/Vps16) or the isotropic equivalent of the anisotropic B-factor and isotropic residual arising from TLS refinement (Vps33/Vps16/Vam3, Vps33/Vps16/Nyv1).